

Description of superdeformed bands in light $N = Z$ nuclei by cranked HFB method

Makito Oi

*Department of Physics, University of Surrey, Guildford, GU2 7XH, Surrey, United Kingdom**

(Dated: August 17, 2007; Ver.1.2)

Superdeformed states in light $N = Z$ nuclei are studied by means of the self-consistent cranking calculation (i.e., the P+QQ model based on the cranked Hartree-Fock-Bogoliubov method). Analyses are given for two typical cases of superdeformed bands in the $A \simeq 40$ mass region, that is, bands where backbending is absent (^{40}Ca) and present (^{36}Ar). Investigations are carried out, particularly for the following points: cross-shell excitations in the sd and pf shells; the role of the $g_{9/2}$ and $d_{5/2}$ orbitals; the effect of the nuclear pairing; and the interplay between triaxiality and band termination.

I. INTRODUCTION

New “islands” of superdeformation (SD) were found, after nearly fifteen years of systematic search, in the nuclear chart around the $A \simeq 40$ mass region (e.g., ^{36}Ar [1] and ^{40}Ca [2]). Surprisingly, these light and symmetric (i.e., $N = Z$) nuclei in the latest SD “archipelago” are magic and near-magic systems, whose ground states have spherical shape.

These light nuclear systems with magic and near-magic numbers need cross-shell excitations, involving both the sd and pf shells, in order to produce collective degrees of freedom necessary for the formation of SD states. The corresponding shell-model space becomes inevitably very large. However, modern high-performance computation systems are quickly advancing to allow shell-model diagonalization to be executed if the minimum and reasonable truncations are justified in the model space.

Mean-field descriptions have a numerical advantage in reducing the dimension over exact diagonalization, owing to the ansatz for a many-body wave function (for example, the Slater determinant in the Hartree-Fock theory). The mean-field approach was exclusively applied [4] to the early studies of SD states known before 2000 [5], such as in the $A \simeq 80$ (e.g., $^{84}\text{Zr}_{44}$ [6]), $A \simeq 150$ (e.g., $^{152}\text{Dy}_{86}$ [7]), and $A \simeq 190$ (e.g., $^{194}\text{Hg}_{114}$ [8]) mass regions. The main reason is that nuclei in these SD archipelagoes belong to heavy- and medium-weight classes. They are still out of reach of the shell-model diagonalization approach using the full model space in the relevant valence shells. The mean-field method has other advantages, particularly related to intuitive understanding of many-body systems, such as nuclear deformation and nuclear superconductivity.

At present, it is true to say that neither mean-field calculations nor truncated shell-model diagonalizations are dominantly superior to their counterpart. They are complementary at the moment. Many theoretical studies using these two approaches followed after the experimental reports were published on ^{36}Ar and ^{40}Ca .

Shell-model diagonalizations were performed by Caugier et al. [1, 9, 10] and Poves [3], with the removal of the $d_{5/2}$ orbital from the sd-pf shells and with the corresponding effective interaction. Recently, they attempted to give a consistent description of the SD and normal deformed states in ^{40}Ca [10]. These calculations with the truncation were very successful in reproducing the experimental energy spectra.

The first attempt through the mean-field approach was carried out with the cranked Nilsson model in the original paper [1]. In the ^{40}Ca paper [2], the cranked RMF (relativistic mean field) method was applied. Both of the methods ignored the pairing correlation, so that the energy spectra of the low-spin members ($J \lesssim 10\hbar$) in the SD bands were not well reproduced.

Long and Sun then applied the projected shell model (PSM). In this model, basis are produced through angular momentum projection onto the Hartree-Fock-Bogoliubov (HFB) states, obtained with the P+Q·Q two-body interaction [11]. A merit in this framework is that the pairing correlation is properly treated. As a consequence, a better agreement was obtained with the experimental data. However, the calculation was restricted to an axial symmetric shape (with the deformation parameter fixed all the way from low- to high-spin regions), so that the shape evolution of the system, particularly the triaxial degree of freedom in response to the Coriolis force, cannot be discussed in this model.

Variable deformation is an important degree of freedom in a rapidly rotating nucleus. For example, the band-termination phenomenon for the SD band is predicted by the cranked Nilsson model, which gives a continuous evolution in triaxiality towards the non-collective oblate deformation ($\gamma = -60^\circ$) in the band limit¹. Inakura et al., applied the cranked Skyrme Hartree-Fock (HF) method, which does not restrict nuclear shape unlike the PSM, but the pairing correlation was ignored [12]. Bender, Flocard, and Heenen analyzed the SD bands in the $A \simeq 40$ region by means of the most sophisticated method, the generator coordinate method (GCM) with

*Electronic address: m.oi@surrey.ac.uk

¹ The sign convention for γ in this study is opposite to the so-called Lund convention.

the projected Skyrme HF+BCS states [13]. The Lipkin-Nogami method and particle number projection were applied, so that the pairing was properly treated. Although nuclear shape can vary through the constraint on the quadrupole moment, only axial deformation was assumed in the calculation. In addition, the analyses were restricted only to low-spin states ($J \leq 6\hbar$). This is because the states with non-zero angular momentum were only kinematically created through angular momentum projection (without cranking). A dynamical effect originating from shape coexistence was considered through the GCM, but the method underestimated the more important dynamical effect coming from the Coriolis force, which plays a major role at high spin.

The aim of this paper is thus to test another mean field approach, which can handle the pairing correlation, the Coriolis force, and the evolution of nuclear shape (in particular, triaxiality) in a fully self-consistent manner, for the full sd-pf model space. For this purpose, the SD bands in ^{36}Ar (a case with backbending) and ^{40}Ca (a case without backbending) are analyzed with the P+Q·Q model based on the HFB method [14], in this work.

II. THE P+Q·Q MODEL OF SELF-CONSISTENT CRANKING CALCULATION

In the current framework, the Hamiltonian contains two terms,

$$\hat{H} = \hat{H}_0 + \hat{V}. \quad (1)$$

The first term \hat{H}_0 represents the one-body term and it is the spherical Nilsson Hamiltonian. In the second quantization notation, it is expressed as

$$\hat{H}_0 = \sum_m e_m a_m^\dagger a_m, \quad (2)$$

where a pair of operators (a_m^\dagger, a_m) denotes fermionic operators of creation and annihilation. This part is solved exactly

$$\hat{H}_0|\psi_m\rangle = e_m|\psi_m\rangle, \quad (3)$$

and the eigenstates $\{|\psi_m\rangle \equiv a_m^\dagger|0\rangle\}$ (the spherical Nilsson states) are used as the basis in the following stages. Index m collectively denotes the quantum numbers in the Nilsson model, that is, $(nlj\Omega)$, as well as isospin and parity. A time-reversal state of m is denoted as \bar{m} . We use the notation “ $m > 0$ ” which means $(nlj; \Omega > 0)$. In this case, its time-reversal state \bar{m} corresponds to $(nlj; -\Omega)$. The so-called Nilsson parameters for the spin-orbit and orbit-orbit forces (denoted as κ and μ in the standard notation) are taken from Refs. [15] and [16].

The second term \hat{V} represents the two-body part, and it is the P+Q·Q interaction in this study,

$$\hat{V} = -\frac{1}{2}\chi \sum_{\mu=-2}^2 \hat{Q}_\mu^\dagger \hat{Q}_\mu - \sum_{\tau=p,n} G_\tau \hat{P}_\tau^\dagger \hat{P}_\tau, \quad (4)$$

where the first and second terms correspond to the particle-hole and particle-particle channels of the two-body interaction, respectively. The former interaction is responsible for the long-range correlation to describe nuclear deformation, while the latter is for the short-range correlation to handle the nuclear pairing. The quadrupole operator and the monopole pairing operator are respectively given as

$$\hat{Q}_\mu = \sum_{mn} (Q_\mu)_{mn} a_m^\dagger a_n, \quad (5)$$

$$\hat{P}_\tau = \sum_{m(\in\tau)>0} a_{\bar{m}} a_m. \quad (6)$$

The Hamiltonian is “diagonalized” with the basis ψ_m , by means of the mean field approximation. It corresponds to a procedure to extract one-body ingredients, \hat{V}_{MF} , from the two-body interaction, \hat{V} , so as to diagonalize \hat{V}_{MF} . The residual part, $\hat{V}_{\text{R}} = \hat{V} - \hat{V}_{\text{MF}}$, is therefore neglected in the approximation.

Remembering that we take the pairing correlation into account, the HFB ansatz is employed in the variational calculations. That is,

$$|\text{HFB}\rangle = \prod_p \beta_p |0\rangle. \quad (7)$$

The quasiparticle annihilation-creation operators (β_p, β_p^\dagger) are related to the original annihilation-creation operators (a_m, a_m^\dagger) through the Bogoliubov transformation,

$$\begin{pmatrix} \beta \\ \beta^\dagger \end{pmatrix} = \begin{pmatrix} U & V^* \\ V & U^* \end{pmatrix} \begin{pmatrix} a \\ a^\dagger \end{pmatrix}. \quad (8)$$

Matrix elements U and V in the Bogoliubov transformation correspond to the variational parameters in the HFB theory. The density matrix ρ and the pairing tensor κ are introduced here, as

$$\rho_{mn} = \langle \text{HFB} | a_n^\dagger a_m | \text{HFB} \rangle = (V^* V^T)_{mn}, \quad (9)$$

$$\kappa_{mn} = \langle \text{HFB} | a_n a_m | \text{HFB} \rangle = (V^* U^T)_{mn}. \quad (10)$$

The mean-field approximation of the Hamiltonian thus reads

$$\begin{aligned} \hat{H}_{\text{HFB}} &= E_{\text{HFB}} + \sum_p E_p \beta_p^\dagger \beta_p \\ &= E_{\text{HFB}} + \sum_{mn} h_{mn} a_m^\dagger a_n + \sum_{\tau=p,n} \sum_{mn \in \tau} \Delta_{mn}^\tau a_m a_n + \text{h.c.} \end{aligned} \quad (11)$$

The one-body component in the particle-hole (ph) channel, represented as h , has the following form.

$$h = e + \Gamma \quad (12)$$

The first term $(e)_{ij} = \delta_{ij} e_i$ represents the spherical Nilsson energy. The second term Γ is called the self-consistent potential,

$$\Gamma_{mn} = \sum_{\mu=-2}^2 q_\mu (Q_\mu)_{mn}, \quad (13)$$

where the self-consistent coefficient q_μ is given as

$$q_\mu = -\chi \text{Tr}(\rho Q_\mu). \quad (14)$$

The coupling constant χ is determined in the standard manner by comparing to the axially deformed Nilsson model with deformation β^0 in the beginning of the variational calculation.

The one-body component in the particle-particle (pp) channel, denoted as Δ in Eq.(11), describes the pairing correlation. It has the form,

$$\Delta_{mn}^\tau = \frac{1}{2} p_\tau^* (P_\tau)_{mn} \quad (\tau = p, n), \quad (15)$$

where the pairing matrix element $(P_\tau)_{mn}$ is determined from Eq.(6) and the self-consistent pairing coefficient p_τ is expressed as

$$p_\tau = -G_\tau \sum_{m(\in\tau)>0} \kappa_{m\bar{m}}. \quad (16)$$

The pairing-gap energy ($\bar{\Delta}$) is defined as the average of the matrix elements of Δ , that is,

$$\bar{\Delta}^\tau \equiv \frac{1}{M'} \sum_{m(\in\tau)>0}^{M'} \Delta_{m\bar{m}}^\tau, \quad (17)$$

where $M' = M/2$ is the half the dimension of a subspace of given isospin (τ). In the case of the present separable interaction, the expression for the pairing gap is simply given as

$$\bar{\Delta}^\tau = p_\tau. \quad (18)$$

The pairing strength G_τ is determined in the standard manner by using the Nilsson+BCS calculation with the initial values for the pairing gaps (Δ^0) together with the β^0 .

High-spin states are produced with the self-consistent cranking model. That is, the variational equation,

$$\delta \langle \text{HFB} | \hat{H} - \omega \hat{J}_x - \sum_{\tau=p,n} \lambda_\tau \hat{N}_\tau | \text{HFB} \rangle = 0, \quad (19)$$

is self-consistently solved by means of the gradient method under the following two constraints:

$$\langle \text{HFB} | \hat{J}_x | \text{HFB} \rangle = \text{Tr}(\rho j_x) = J, \quad (20)$$

where J is the total angular momentum, and

$$\langle \text{HFB} | \hat{N} | \text{HFB} \rangle = \text{Tr}(\rho) = N, \quad (21)$$

where N is the total particle number.

In this study, the usual one-dimensional cranking model is implemented, so that only one component of the total angular momentum vector is constrained. Quantities ω and λ_τ in the variational equation are the Lagrange multipliers. The first multiplier is interpreted as the rotational frequency, while the second multiplier stands for

the chemical potential. The presence of the chemical potential is due to the introduction of the BCS-type pairing correlation, which breaks the particle number conservation. As a result, the mean particle number needs to be constrained in the calculation.

The HFB energy E_{HFB} can be thus written as

$$E_{\text{HFB}}^J = \langle \text{HFB}(J) | \hat{H} | \text{HFB}(J) \rangle = \text{Tr}(\rho h) - \sum_{\tau=p,n} \bar{\Delta}_\tau^2, \quad (22)$$

and this corresponds to the yrast spectrum.

For the model space, two major shells ($N = 2, 3$, or the so-called sd-pf shell) each for protons and neutrons are used, that is, $d_{5/2}, s_{1/2}, d_{3/2}$ ($N = 2$); $f_{7/2}, p_{3/2}, f_{5/2}, p_{1/2}$ ($N = 3$). This choice is in accordance with the Kumar-Baranger prescription for the P+Q·Q force [17]. When a role of an intruder $g_{9/2}$ ($N = 4$) orbital is discussed, it is also included in the model space.

Further details of the method are available in Ref.[14].

III. NUMERICAL RESULTS

Two $N = Z$ nuclear systems will be studied in this paper, which are ^{40}Ca and ^{36}Ar . The former nucleus shows no sign of backbending so far (up to $J = 16\hbar$), while the latter has a clear backbending at $J = 10\hbar$. With the P+Q·Q model based on the cranked HFB approach, we attempt to describe the superdeformed states in these nuclei in a self-consistent manner both in the ph- and pp-(hh-) channels.

A. A case of no backbending: ^{40}Ca

The SD band of ^{40}Ca is so far identified up to $J = 16\hbar$ [2]. This rotational band is regular and no backbending is currently observed.

1. A role of the $d_{5/2}$ orbital

As stated above, our model space contains the full sd- and pf-shells. It is thus possible to examine, in the framework of the self-consistent mean-field calculation, the core-polarization effect, or the influence coming from the $d_{5/2}$ orbital truncated in the shell-model calculations. The occupation numbers of each single-particle orbital provides us useful information for this aim.

Before analyzing our own calculations, it is worth learning the results obtained by others. In a description of the SD band of ^{40}Ca through the shell-model diagonalization by Poves [3], the single-particle model space is set to be $s_{1/2}, d_{3/2}$ ($N = 2$); $f_{7/2}, p_{3/2}, f_{5/2}, p_{1/2}$ ($N = 3$). (This choice of the model space was also used for ^{36}Ar .) The $d_{5/2}$ orbital is excluded from the valence space for the numerical reason. Within this model space (and the

corresponding effective interaction), the 8p-8h configuration, that is, $(s_{1/2}d_{3/2})^4(\text{fp})^8$, was proposed for the description of the SD band. The calculated result based on this configuration reproduces the experimental data quite well with a well-tuned effective interaction [1, 3]. Long and Sun raised the question about the $d_{5/2}$ truncation in their paper where they performed the PSM (projected shell model) calculation[11]. According to their analysis, the $d_{5/2}$ orbital does not contribute to the SD state in ^{36}Ar , but to higher excited rotational bands. The cranked Nilsson calculation performed for ^{36}Ar [1] is also informative. It was obtained that only about half a particle in each isospin sector is excited into higher orbitals from the $d_{5/2}$ orbital. Summarizing these results, it can be said that Poves' prescription for the truncation might be a good approximation for a description of the SD band.

Now, let us turn to our calculation. The initial parameters for the self-consistent iterations are chosen to be $\beta^0 = 0.6$ and $(\Delta_p^0, \Delta_n^0) = (1.360, 1.513)$ MeV. These initial pairing-gap energies are employed from Ref. [18].

In Fig. 1, the average occupation numbers, which are diagonal elements of the density matrix, ρ , are presented as a function of the total angular momentum. The right and left panels in the figure show the occupation numbers for protons and neutrons, respectively. The graphs look quite similar to each other as a consequence of $N = Z$. Following the presentation in Ref. [1], the occupation in the $d_{5/2}$ orbital is plotted using the hole occupation number. Our result shows (see Table I) that only half a particle is missing from the fully filled $d_{5/2}$ orbital, which supports the shell-model truncation by Poves. This result is similar to the cranked Nilsson calculation for ^{36}Ar [1]. However, the number increases at higher spin ($J \gtrsim 16\hbar$) to reach to 1 (see Table II), so that the core polarization may need to be taken into account, particularly at high spin.

Orbital	$d_{5/2}$	$s_{1/2}$	$d_{3/2}$	$f_{7/2}$	$p_{3/2}$	$f_{5/2}$	$p_{1/2}$
Proton	5.48	1.01	1.54	2.63	0.88	0.29	0.17
Neutron	5.45	1.03	1.56	2.55	0.92	0.30	0.19
Total	10.93	2.04	3.10	5.18	1.80	0.59	0.36

TABLE I: Occupation numbers of ^{40}Ca at $J = 0$. The subspace $(s_{1/2}d_{3/2})$ is occupied by about five ($= 5.14$) particles, while the pf-shell is filled with about eight ($= 7.93$) particles. The hole occupation number in the $d_{5/2}$ orbital is 1.07 ($= 12 - 10.93$).

Table I displays the details of the occupation numbers at $J = 0$. The net occupation number in the $d_{5/2}$ orbitals are 10.93, that is, about one particle (in the isoscalar basis) is excited into upper orbitals, as already mentioned above. The total numbers of the occupation in the subspace $(s_{1/2}d_{3/2})$ and the pf shell ($f_{7/2}p_{3/2}f_{5/2}p_{1/2}$) are about five and eight, respectively. In other words, our calculation suggests $(d_{5/2})^{-1}(d_{3/2}s_{1/2})^5(\text{fp})^8$ for the

Orbital	$d_{5/2}$	$s_{1/2}$	$d_{3/2}$	$f_{7/2}$	$p_{3/2}$	$f_{5/2}$	$p_{1/2}$
Proton	5.11	1.22	1.67	2.68	0.57	0.52	0.23
Neutron	5.11	1.22	1.64	2.64	0.61	0.50	0.24
Total	10.22	2.44	3.31	5.32	1.18	1.02	0.47

TABLE II: Occupation numbers of ^{40}Ca at $J = 18\hbar$. The subspace $(s_{1/2}d_{3/2})$ is occupied by about six ($= 5.75$) particles, while the pf shell is filled with about eight ($= 7.99$) particles. The hole occupation number in the $d_{5/2}$ orbital is 1.78 ($= 12 - 10.22$).

band-head structure of the SD band. To a good extent, this configuration is consistent with the 8p-8h structure proposed in the shell-model calculation. Although our calculation indicates a possible core polarization, this effect can be minor at low spin.

Table II shows the occupation numbers at $J = 18\hbar$. The number of particles in the pf shell is maintained to be eight ($= 7.99$), but about one more particle is excited from the $d_{5/2}$ to the $(s_{1/2}d_{3/2})$ subspace. The corresponding configuration is thus approximated as $(d_{5/2})^{-2}(d_{3/2}s_{1/2})^6(\text{fp})^8$.

Comparing these two tables (and also from Fig.1), it can be seen that the rotational band is created through two modes. One is excitation within the sd shell, mainly an excitation from the $d_{5/2}$ orbital to the upper sd shell ($s_{1/2}d_{3/2}$); the other is within the pf shell and the relevant excitation is mainly from the $p_{3/2}$ orbital to the $f_{5/2}$ orbital. It is also learned from the calculations that the numbers of particles in the $f_{7/2}$ and the $d_{3/2}$ orbitals are almost constant in a wide range of the total angular momentum.

From the above analysis, it can be said that the main part of the superdeformed structure is determined by the eight particles in the pf shell. Whereas, rotational members of the SD band are mainly produced by gradual excitations from the $d_{5/2}$ orbital to the upper sd shell in our model, in addition to the minor internal reconfiguration inside the pf shell.

2. A role of the $g_{9/2}$ orbital in $J \leq 16\hbar$ and rotational energy

It is worth examining here an effect of the $g_{9/2}$ orbital ($N = 4$), which is missing from the shell model calculation.

Let us see first the calculated rotational energy of the SD band with the original single-particle model space, that is, without the $g_{9/2}$ orbital. The calculated and observed spectra of the SD band are plotted in Fig.2. The band-head ($J = 0$) energy of the calculated spectrum is normalized with the experimental data, $E(J = 0) = 5.218$ MeV. The agreement looks very good, particularly at low spin ($J \lesssim 12\hbar$). In Fig.3, the excitation energy is plotted, following Ref.[2], relative to a rigid rotor energy,

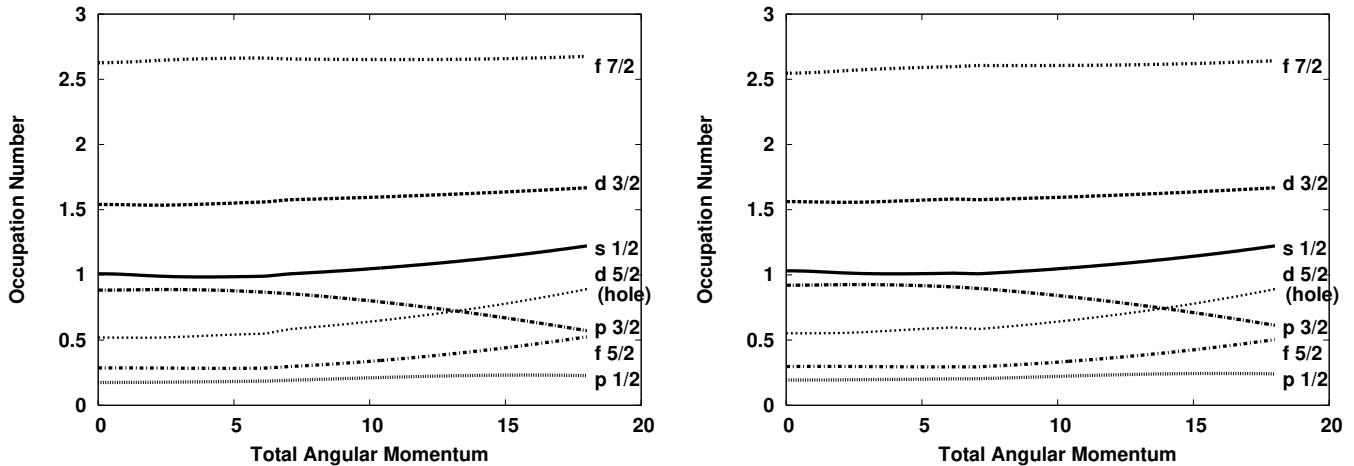


FIG. 1: Proton (left) and neutron (right) occupation numbers as a function of the total angular momentum for ^{40}Ca . In this case, the $g_{9/2}$ orbital is excluded from the model space.

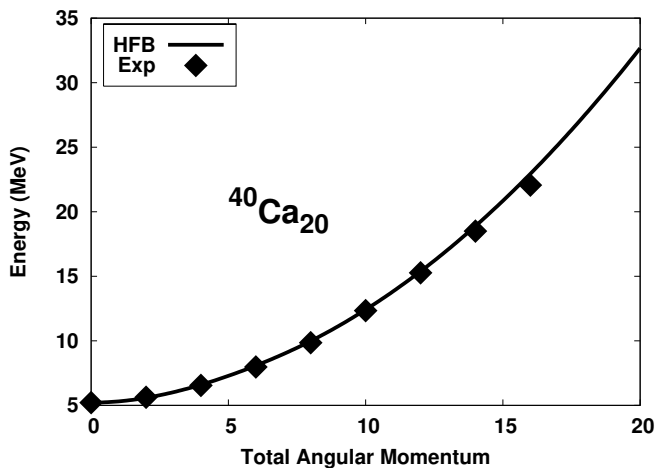


FIG. 2: Calculated and observed rotational energy of the SD band in ^{40}Ca . The calculated ground-state energy (at $J = 0$) is normalized with the experimental value, $E(J = 0) = 5.218$ MeV.

$E_R = 0.06909 J(J + 1)$ [MeV] (with a line labeled as HFB-Np, which is performed in the absence of the $g_{9/2}$ orbital in the model space).

Despite this good agreement, the role of the $g_{9/2}$ orbital is still worth an examination because the (deformed) Nilsson model implies that some of the split $g_{9/2}$ states intrude into the sd shell ($N = 2$) at $\beta \simeq 0.6$. (See, for example, Fig 2.21a, p.73 in Ref.[19].) For this purpose, the $g_{9/2}$ orbital is added to the model space in the present framework, and the calculation is repeated with the pairing force being unchanged. The result is plotted with a line denoted as HFB-Gp in Fig. 3. The low-spin behavior is almost identical to the previous case (HFB-Np), that is, without the $g_{9/2}$ orbital. A small deviation from the HFB-Np can be seen at high spin ($J \gtrsim 12\hbar$), but in practice this difference is negligible as far as the

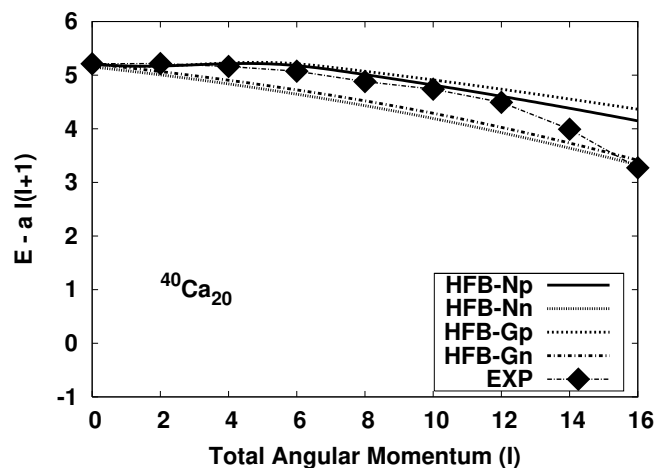


FIG. 3: Excitation energies relative to a rigid-rotor energy, $E_R = aJ(J + 1)$, where $a = 0.06909$ (MeV) for ^{40}Ca . The four calculated results (HFB-Np, Nn, Gp, and Gn) are compared with the experimental data. The HFB calculations with (without) the $g_{9/2}$ orbital are denoted as G (N). In addition, two different sets of the initial value for the pairing are chosen for each case. The set p corresponds to $(\Delta_p^0, \Delta_n^0) = (1.360, 1.513)$ MeV, while the set n to $(\Delta_p^0, \Delta_n^0) = (0.15, 0.15)$ MeV.

rotational energy is concerned. The occupation numbers are also plotted in Fig.4, which shows only slight differences from Fig.1. It looks that the inclusion of the $g_{9/2}$ orbital gives rise to only a minor influence to the nuclear structure, but it turns out to be quite essential to the high-spin nuclear structure of ^{40}Ca , through the subsequent analyses. We will come back to this argument in connection to backbending.

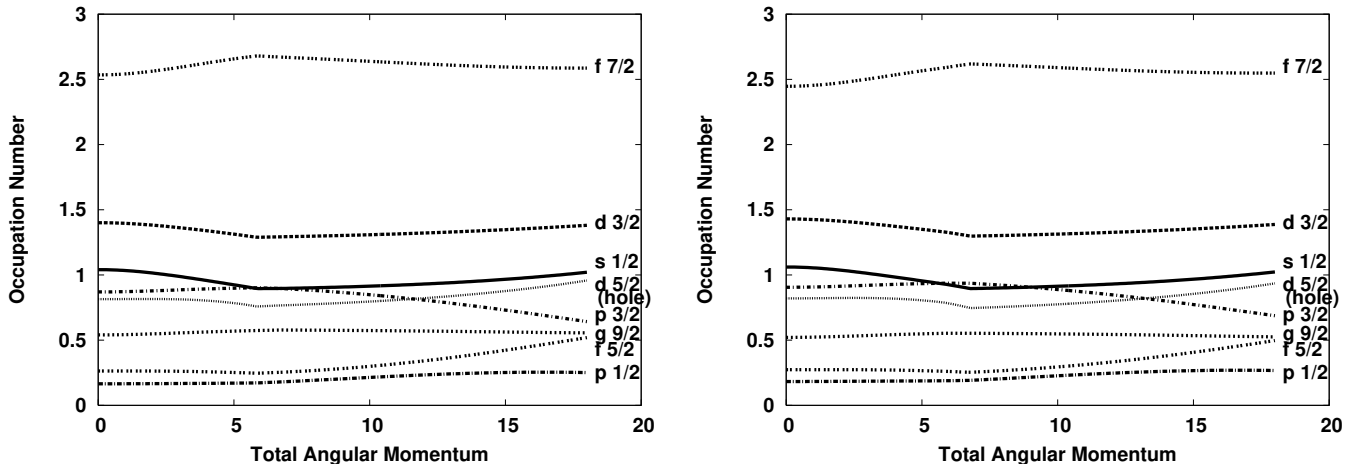


FIG. 4: Proton (left) and neutron (right) occupation numbers as a function of the total angular momentum for ^{40}Ca . In this case, the $g_{9/2}$ orbital is included in the model space.

3. An effect of pairing correlation and backbending

An effect of the pairing correlation can be also studied here. Our approach here is to compare two cases: with and without the pairing. The case without the pairing is constructed by choosing the initial pairing-gap energies to be small: $(\Delta_p^0, \Delta_n^0) = (0.150, 0.150)$ [MeV]. With this choice, the gap energies disappear as early as $J \simeq 0.1\hbar$ and remain to do so at higher spin. This calculation is essentially the Hartree-Fock (HF) calculation without the pairing, like the cranked RMF [2] and the cranked Skyrme HF [12].

The rotational energies in Fig.3 denoted HFB-Nn and HFB-Gn correspond to the case with and without the $g_{9/2}$ orbital, respectively (the both cases are without the pairing). As seen in the figure, there is no much difference between these two cases, but the both of them underestimate the experimental data. When the pairing is adequately taken into account (HFB-Np and HFB-Gp), there is a plateau structure in the graph at low-spin region, which brings a better agreement to the experimental data. However, when the pairing correlations are absent, the plateau structure disappears and the steeper curves appear. The similar results were obtained in the other mean-field calculations neglecting the pairing correlation, such as the cranked RMF model [2] and the cranked Skyrme HF calculation [12]. In the case of ^{36}Ar , the shell model calculation [1] and the PSM [11] reproduce the experimental data fairly well, and the plateau structure is seen in these calculations. These results suggest the importance of the higher order correlations in the two-body interaction beyond the mean-field level. However, our calculation also implies that an inclusion of the pp-channels in the mean-field approximation, that is, the pairing correlations, seem to “salvage” effectively the important correlations that the ph-channels in the mean-field approximation fail to pick up. To support

this remark, discrepancies in the excitation energy start to happen (which is of the order of about 1 MeV), after the gap energies disappear at $J \gtrsim 6 - 7\hbar$ (See Figs.3 and 5, as well as the subsequent discussion in the following paragraph).

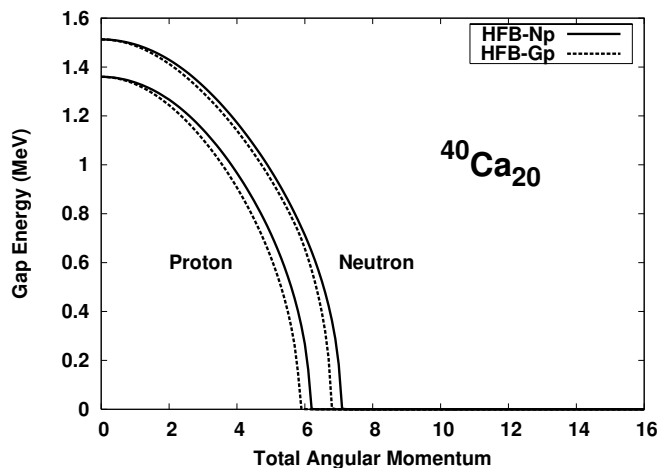


FIG. 5: Calculated pairing-gap energies as a function of the total angular momentum for ^{40}Ca . The identification of the curves are the same as Fig.3.

Fig.5 displays the calculated pairing-gap energies for protons and neutrons with the original initial values for $(\Delta_p^0, \Delta_n^0) = (1.360, 1.513)$ MeV. In either case, the gap energies disappear at $J \gtrsim 8\hbar$, which is roughly consistent with the point where the deviation in the calculated excitation energy can be seen in Fig.3. In finite systems, the pairing correlation should persist even at high spin, like in the Fig.2(d) in Ref.[11]. This “collapse” of the pairing is a notorious problem in the BCS-type theory applied to a finite system, and this “phase transition” of the pairing gap is known to be a mere artifact of the model. In

reality, nuclear systems should undergo a crossover, or a gradual decrease in the pairing gap. In the present work, the disappearance of the calculated gap energies is rather smooth and gradual, so that the qualitative feature of the system might be expected to be maintained, as Ring and Schuck explain at p.278 in their textbook [19]. However, a more elaborate treatment to keep the pairing correlation is necessary for more accurate descriptions at high spin, such as the Lipkin-Nogami method [20].

So far, no backbending is reported in the SD band of ^{40}Ca (until $J = 16\hbar$), and our calculation is consistent with this observation (with or without an inclusion of the $g_{9/2}$ orbital). The shell model calculation by Poves also reproduced this result. Interestingly, the shell model calculation predicts the backbending at higher spin ($J \simeq 20\hbar$) [3]. This angular momentum corresponds to the band termination for the 8p-8h configuration, that is, $(d_{3/2}s_{1/2})^4(f_{7/2})^8$. According to Poves, the nuclear structure after the backbending is constructed by such configurations as $(d_{3/2}s_{1/2})^4(f_{7/2})^7p_{3/2}$, as well as similar configurations allowing excitations into higher orbitals in the pf shells.

In order to see clearly how backbending occurs, the so-called “backbending plot” is convenient. In this paper, the transition energy, $E_\gamma(J)$, is defined as

$$E_\gamma(J) \equiv E(J) - E(J-2), \quad (23)$$

where $E_\gamma(0) = 0$. Alternatively, the rotational frequency is defined as

$$\omega(J) = E_\gamma(J)/2\hbar, \quad (24)$$

and $\omega(0) = 0$.

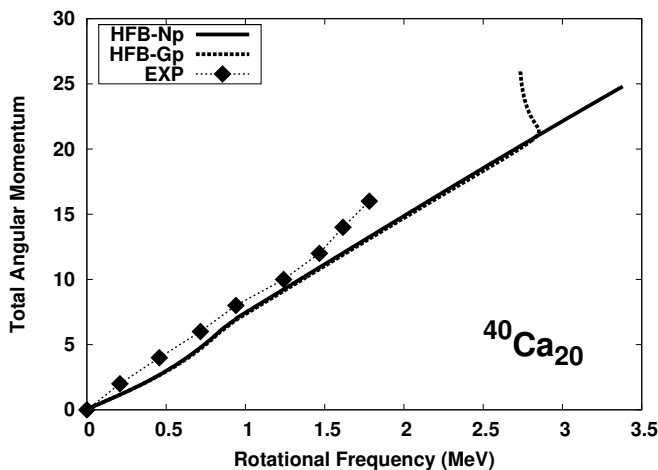


FIG. 6: Backbending plot of the SD band of ^{40}Ca . HFB-Np (HFB-Gp) corresponds to the calculation without (with) the $g_{9/2}$ orbital in the model space.

In Fig.6, two cases of the calculations are plotted (with and without the $g_{9/2}$ orbital). The line denoted by HFB-Np (HFB-Gp) corresponds to the case without (with) the $g_{9/2}$ orbital in the model space. As confirmed in

Figs.1 and 4, there is no much difference between these two cases in the spin range $J \lesssim 20\hbar$. This situation is reflected in Fig.6 showing completely the same behaviors in the two calculated lines in $J \lesssim 20\hbar$. A difference happens beyond $J = 20\hbar$. The case without the $g_{9/2}$ orbital (HFB-Np) shows no sign of backbending even at as high as $J = 25\hbar^2$, while the line of HFB-Gp starts to backbend at $J = 20\hbar$, as predicted by the shell model calculation. However, it should be noted that the shell model calculation does not contain the $g_{9/2}$ and $d_{5/2}$ orbitals.

4. A role of the $g_{9/2}$ orbital in the backbending

To study the rotational alignment, it is useful to calculate the single-particle angular momentum component along the cranking axis. The quantity is given as

$$\langle j_x(m) \rangle = \sum_n \rho_{mn} (j_x)_{nm}, \quad (25)$$

where the indices m, n denote the spherical Nilsson basis.

Fig.7 shows the single-particle spin component along the cranking axis, in the case where the $g_{9/2}$ orbital is excluded from the model space. The $f_{7/2}$ orbital is the major contributor to the total angular momentum, and its contribution becomes gradually increased at higher spin states. About 60% of the total angular momentum is produced by this orbital (of protons and neutrons). The second main component is produced by the $d_{5/2}$ orbitals, and its percentage to the total angular momentum reaches nearly 20% at $J = 25\hbar$. The contributions from the $d_{3/2}$ and $f_{5/2}$ orbitals are also significant at high spin.

Fig.8 shows the single-particle spin components when the $g_{9/2}$ orbital is included in the model space. Beyond $J = 20\hbar$, a clear structural change is seen. That is, the contributions from the $f_{7/2}$ orbital as well as $d_{3/2}$ and $f_{5/2}$ orbitals are saturated. Instead, a rapid alignment of the $g_{9/2}$ orbital happens. Obviously, the backbending seen in Fig.6 is caused by this structural change. As mentioned earlier, in the case of the shell model calculation, backbending is initiated by the band termination, $(d_{3/2}s_{1/2})^4(f_{7/2})^8$. The higher spin states are produced as excitations happen from the $f_{7/2}$ orbital to higher orbitals in the pf shell. Comparing with our results, the backbending occurs from similar reasons, but not exactly the same. First of all, the direct factor to cause the backbending is the rapid alignment in the $g_{9/2}$ orbital, which corresponds to an excitation to higher orbitals, but this excitation is more drastic in the sense that three major

² The calculation of HFB-Np can be executed up to $J \simeq 25\hbar$. Beyond this angular momentum, the SD structure no longer exists in the current framework. The cranked Skyrme HF calculation by Inakura, et al. also shows that the SD structure ends at $J = 24\hbar$.

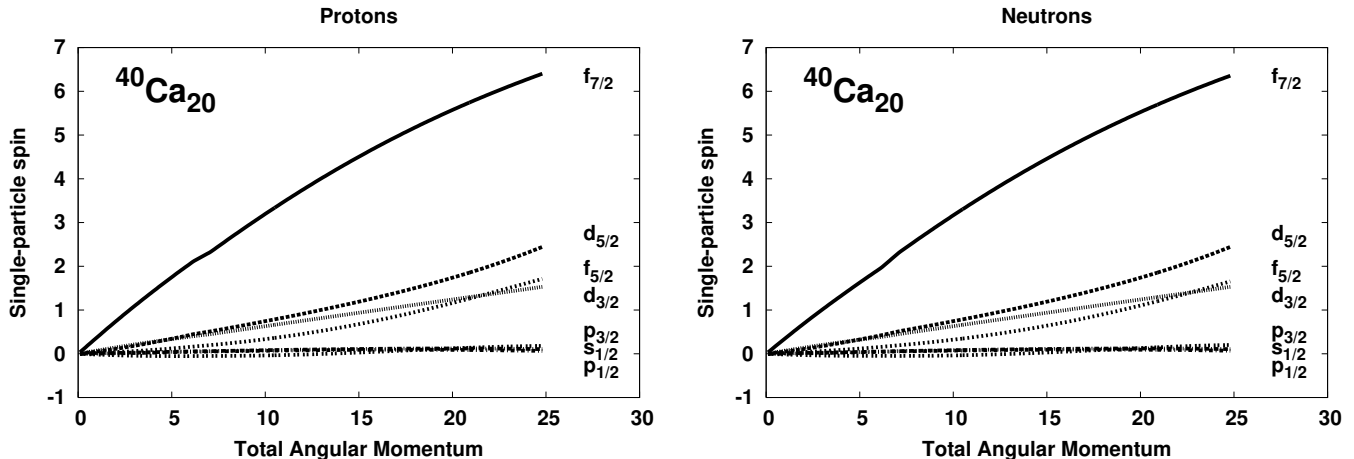


FIG. 7: Proton (left) and neutron (right) single-particle spin components along the cranking axis for ^{40}Ca . In this case, the $g_{9/2}$ orbital is excluded from the model space.

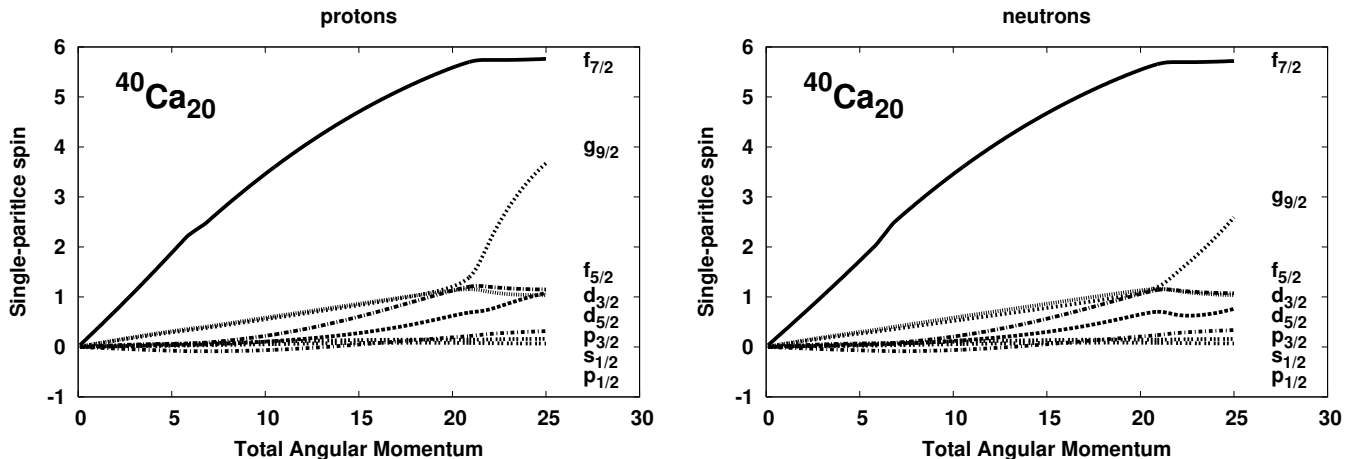


FIG. 8: Proton (left) and neutron (right) single-particle spin components along the cranking axis for ^{40}Ca . In this case, the $g_{9/2}$ orbital is included in the model space.

shells are involved (i.e., sd-pf-g). In addition, the saturation of the alignment in the $f_{7/2}$ orbital produces the similar mechanism as the band termination. In fact, the maximum angular momentum generated by two particles occupying the $f_{7/2}$ orbital is $6\hbar$, which is almost the value read in Fig.8 for the $f_{7/2}$ orbital. Unlike the simple band termination picture, the $d_{3/2}$ and $f_{5/2}$ orbitals also show the saturation, despite that the generated angular momenta are less than the maximum values. No more additional angular momentum is created by further alignments of these orbitals in the sd and pf shells beyond $J = 20\hbar$ (i.e., before the backbending). In other words, beyond this total angular momentum, only one high- j orbital ($g_{9/2}$) dominantly produces an additional angular momentum on top of the collective angular momentum already produced by the particles in the sd and pf shells. This mechanism is exactly the same as the

original backbending mechanism in the rare-earth nuclei, where the $i_{13/2}$ orbital (usually, of neutrons) plays the same role as its counterpart, that is, the $g_{9/2}$ orbital.

The calculated occupation numbers (Tables III and IV) imply that the configuration changes from $(d_{5/2})^{-2}(d_{3/2}s_{1/2})^5(fp)^8(g_{9/2})^1$ to $(d_{5/2})^{-3}(d_{3/2}s_{1/2})^5(fp)^8(g_{9/2})^2$ in the backbending region. Essentially, this change is brought by an excitation from the $d_{5/2}$ orbital to the $g_{9/2}$ orbital, while the configurations inside the pf shell and the subspace of the sd shell are relatively stable throughout the whole range of angular momentum. This excitation from the $d_{5/2}$ orbital to the $g_{9/2}$ orbital can be understood through the Nilsson diagram around $\beta \simeq 0.6$. There, a low- Ω component originating from the $g_{9/2}$ orbital, that is, $[440]_{1/2}$, behaves like an intruder orbital coming down to the region near the $d_{5/2}$ and $d_{3/2}$ orbitals. This situation

Orbital	d _{5/2}	s _{1/2}	d _{3/2}	f _{7/2}	p _{3/2}	f _{5/2}	p _{1/2}	g _{9/2}
Proton	5.04	1.02	1.38	2.59	0.64	0.52	0.25	0.56
Neutron	5.06	1.02	1.39	2.55	0.69	0.50	0.27	0.53
Total	10.10	2.04	2.77	5.14	1.33	1.02	0.52	1.09

TABLE III: Occupation numbers of ^{40}Ca at $J = 18\hbar$ in the case with the $g_{9/2}$ orbital included in the model space. The subspace ($s_{1/2}d_{3/2}$) is occupied by about five ($= 4.81$) particles, while the pf shell is filled with about eight ($= 8.01$) particles. The hole occupation number in the $d_{5/2}$ is 1.90 ($= 12 - 10.10$).

Orbital	d _{5/2}	s _{1/2}	d _{3/2}	f _{7/2}	p _{3/2}	f _{5/2}	p _{1/2}	g _{9/2}
Proton	4.46	1.00	1.39	2.49	0.66	0.59	0.26	1.16
Neutron	4.65	0.99	1.40	2.45	0.71	0.56	0.28	0.96
Total	9.11	1.99	2.79	4.94	1.37	1.15	0.54	2.12

TABLE IV: Occupation numbers of ^{40}Ca at $J = 26\hbar$ in the case with the $g_{9/2}$ orbital included in the model space. The subspace ($s_{1/2}d_{3/2}$) is occupied by about five ($= 4.78$) particles, while the pf shell is filled with eight ($= 8.00$) particles. The hole occupation number in the $d_{5/2}$ is 2.89 ($= 12 - 9.11$).

implies that these three positive-parity states can jointly compose the nuclear many-body state when the system undergoes superdeformation. To produce high angular momentum, it is efficient to place more particles into the $g_{9/2}$ orbital.

It is worth studying more closely the case without the $g_{9/2}$ orbital, in which our calculation shows no sign of backbending. From Tables V and VI, the configuration at high spin looks quite stable to keep the structure of $(d_{5/2})^{-2}(d_{3/2}s_{1/2})^6(\text{fp})^8$. The rotational members in the band are produced through gradual excitations from the $d_{5/2}$ orbital to the upper sd shell as well as a minor rearrangement within the pf shell. In other words, this structural change is adiabatic against the increment of the Coriolis force. This adiabatic nature of the high-spin nuclear structure is nothing but to mean the regularity of the band. In this way, no backbending is seen in this case. Fig.7 shows that the total angular momentum is created

Orbital	d _{5/2}	s _{1/2}	d _{3/2}	f _{7/2}	p _{3/2}	f _{5/2}	p _{1/2}
Proton	5.02	1.29	1.70	2.70	0.50	0.59	0.21
Neutron	5.02	1.29	1.70	2.66	0.54	0.56	0.23
Total	10.04	2.58	3.40	5.36	1.04	1.15	0.44

TABLE V: Occupation numbers of ^{40}Ca at $J = 20\hbar$ in the case with the $g_{9/2}$ orbital excluded from the model space. The subspace ($s_{1/2}d_{3/2}$) is occupied by about six ($= 5.98$) particles, while the pf shell is filled with about eight ($= 7.99$) particles. The hole occupation number in the $d_{5/2}$ orbital is 1.96 ($= 12 - 10.04$).

Orbital	d _{5/2}	s _{1/2}	d _{3/2}	f _{7/2}	p _{3/2}	f _{5/2}	p _{1/2}
Proton	4.78	1.46	1.77	2.75	0.35	0.73	0.17
Neutron	4.78	1.46	1.77	2.72	0.39	0.71	0.18
Total	9.56	2.92	3.54	5.47	0.74	1.44	0.35

TABLE VI: Occupation numbers of ^{40}Ca at $J = 26\hbar$ in the case with the $g_{9/2}$ orbital excluded from the model space. The subspace ($s_{1/2}d_{3/2}$) is occupied by about five ($= 6.46$) particles, while the pf shell is filled with eight ($= 8.00$) particles. The hole occupation number in the $d_{5/2}$ orbital is 2.44 ($= 12 - 9.56$).

mainly through the gradual and monotonic alignment in the $f_{7/2}$ orbital. In addition, the contributions of the $d_{3/2}$ and the $f_{5/2}$ orbitals are seen to be non-negligible, as shown in the shell model calculation. As in the previous case, the $d_{5/2}$ orbital also contributes to the creation of the total angular momentum.

5. Evolution of shape

Finally, let us examine how shape evolution happens in our calculation. To show quadrupole deformation, the Hill-Wheeler coordinates (β, γ) [21] are used in this work. That is, $\langle \hat{Q}_0 \rangle \propto \beta \cos \gamma$ and $\langle \hat{Q}_2 \rangle \propto \beta \sin \gamma / \sqrt{2}$. In the P+Q·Q model, the proportional constant carrying the unit of the quadrupole moment is given as $(\hbar\omega/\hbar c)^2 mc^2 \chi^{-1}$, where the harmonic oscillator energy is $\hbar\omega = 41A^{-1/3}$ (MeV), and $\hbar c = 197$ (MeV·fm). The mass for a nucleon is $mc^2 \simeq 1$ (GeV) and the coupling constant χ is given in Eq.(14).

Fig.9 presents the calculated triaxiality (γ) and elongation (β) for the two cases (with and without the $g_{9/2}$ orbital, which are respectively denoted as HFB-Gp and HFB-Np, in the figure). Until $J = 20\hbar$, the elongation does not change significantly. The higher the total angular momentum, the more shrinkage of the deformation can be seen along the longest principal axis of the quadrupole moment. But the two curves start to deviate from each other beyond the angular momentum $J = 20\hbar$. The curve corresponding to the case without the $g_{9/2}$ orbital (HFB-Np) shows a monotonic decrease to reach $\beta \simeq 0.42$, while the curve corresponding to the case with the $g_{9/2}$ orbital (HFB-Gp) stops decreasing at $J = 20\hbar$ to maintain the deformation larger than $\beta = 0.55$. The shell model calculation by Poves [3] also implies the shrink of the shape until $J = 18\hbar$ in the calculation of the intrinsic quadrupole moment, Q_0 . The cranked Skyrme-HF calculation by Inakura et al. [12] also shows the shrink, and the elongation is demonstrated to keep $\beta \gtrsim 0.5$ (for $J \leq 24\hbar$) for the three parameter sets (SIII, SkM*, SLy4). This result is consistent with our HFB-Gp case, that is, the case with the $g_{9/2}$ orbital (and with the non-vanishing initial pairing-gap parameters).

On the contrary to the elongation, there is a significant

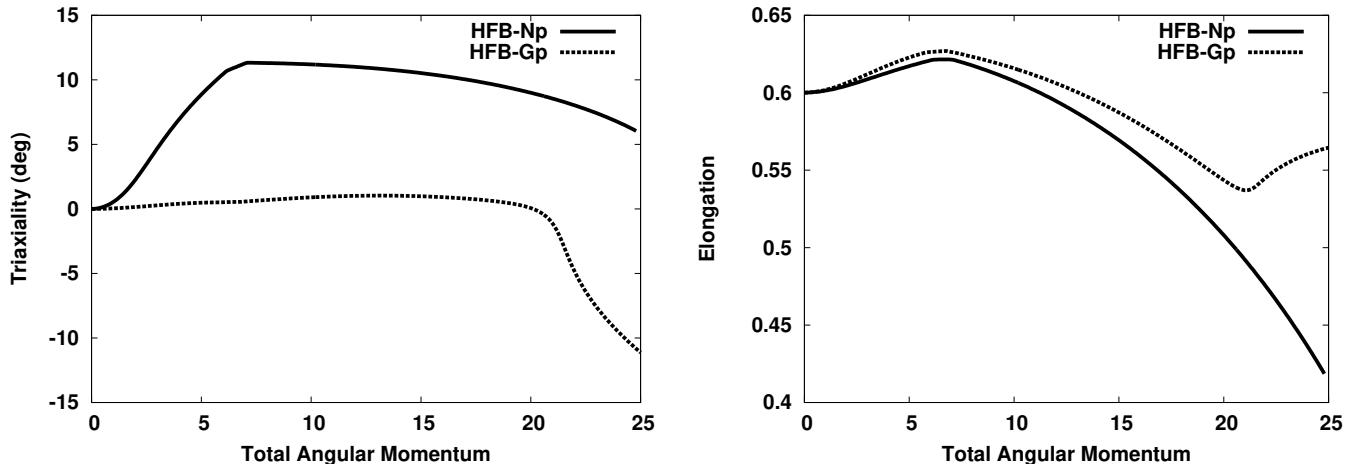


FIG. 9: Calculated triaxiality γ (left panel) and elongation β (right), as functions of the total angular momentum for ^{40}Ca . Captions HFB-GP and HFB-NP denote the cases with and without the $g_{9/2}$ orbital, respectively.

difference in the triaxiality between the two cases (i.e., with and without the $g_{9/2}$ orbital). The case without the $g_{9/2}$ orbital shows that the triaxiality is always positive ($\gamma > 0^\circ$) and the triaxial deformation already starts to grow at low spin although the triaxiality is not so large ($0^\circ \lesssim \gamma \lesssim 10^\circ$). The other case (with the $g_{9/2}$ orbital) shows that the nucleus is axially symmetric until the backbending starts at $J = 20\hbar$. Beyond the backbending angular momentum ($J = 20\hbar$), the triaxiality quickly starts to grow with negative values, which are consistent with the picture of the band termination. The amount of triaxiality is, however, not so substantial ($|\gamma| \lesssim 10^\circ$) even at $J \simeq 25\hbar$. The cranked Skyrme-HF calculation [12] gave the consistent results with our calculation for the case with the $g_{9/2}$ orbital, that is, the γ is negative and the amount (an absolute value of γ) is less than 10° for $J \leq 24\hbar$.

6. Summary for ^{40}Ca

Let us summarize here our analysis on the SD states of ^{40}Ca . The structure of the SD band of ^{40}Ca is mainly determined by the eight particles placed in the pf shell. About five to six particles sit in the $(s_{1/2}d_{3/2})$ subspace of the sd shell, which corresponds to the configuration of six to seven holes. The truncation of the $d_{5/2}$ orbital in the shell model calculation demands the eight-hole configuration in the subspace, which is approximately consistent with our result. However, for more accurate descriptions, the $d_{5/2}$ and $g_{9/2}$ orbitals need to be taken into account in the model space. This is particularly so for the description of the nuclear structure at high spin ($J \gtrsim 20\hbar$), where the backbending is predicted.

In the presence of these additional orbitals, the phenomenon similar to the band termination starts to occur at $J = 20\hbar$ in our model, but the saturation of align-

ments in the pf and sd shells are assisted by the quick alignment in the $g_{9/2}$ orbital, to which particles are excited from the $d_{5/2}$ orbital. This mechanism is consistent with the deformed Nilsson model, where the $g_{9/2}$ orbital comes down to the sd shell, as an “intruder” orbital at superdeformation ($\beta \simeq 0.6$). As a result of the saturation of the spin alignment in the sd-pf shell and the quick alignment of the $g_{9/2}$ orbital, triaxial deformation starts occur, but its amount is not so substantial ($|\gamma| \lesssim 10^\circ$) that one can conclude that the nucleus keeps near-axial symmetry with superdeformation ($\beta \simeq 0.6$).

B. A case of backbending : ^{36}Ar

The second targeted nucleus in this paper, ^{36}Ar , shows a backbending at $J = 10\hbar$ in its superdeformed band, which is currently identified up to $J = 16\hbar$ [1]. The $(s_{1/2}d_{3/2})^4(pf)^4$ structure is proposed in the shell model calculation truncating the $d_{5/2}$ orbital [1]. For the cause of the backbending, simultaneous alignments of protons and neutrons in the $f_{7/2}$ orbitals were suggested by the PSM [11].

1. Deformation of the band head

There are slight disagreements in the calculated band-head deformation among different models. In the calculation with the cranked Nilsson model, minimization of the potential energy surface $E(\gamma, \beta)$ gave $\beta \simeq 0.45$ and $\gamma = 0^\circ$ for the band head [1]. The PSM calculation assumed axial symmetry ($\gamma = 0^\circ$) and the fixed value $\beta \simeq 0.48$, no matter how high (or low) the total angular momentum is [11]. The calculations with the cranked Skyrme HF (the SIII and SkM* parameteriza-

tions for the interaction ³⁾ resulted in $\beta \simeq 0.5$ and $\gamma = 0^\circ$ [12]. In the calculation done by Bender, et al. assuming axial symmetry[4], there was no SD minimum found in their mean-field solution (The Skyrme HF+BCS with the SLy6 force parameterization), but the projected solutions gave rise to the minimum at $\beta \simeq 0.5$.

Considering these calculations, the initial deformation parameter $\beta^0 = 0.5$, as well as axial symmetry ($\gamma^0 = 0^\circ$), seems reasonable for our initial deformation parameters. The initial pairing-gap energies are employed to be $(\Delta_p^0, \Delta_n^0) = (1.70, 1.65)$ MeV, which are about 6% stronger than the values suggested in Ref.[18]. This adjustment is made so as to avoid the sudden disappearance of the gap energy. With this slight modification, the gap energy turns to disappear more gradually and smoothly at $J \simeq 7\hbar$, as shown in Fig.10. We have confirmed, however, that the overall qualitative nature of the SD state are unchanged for the modification.

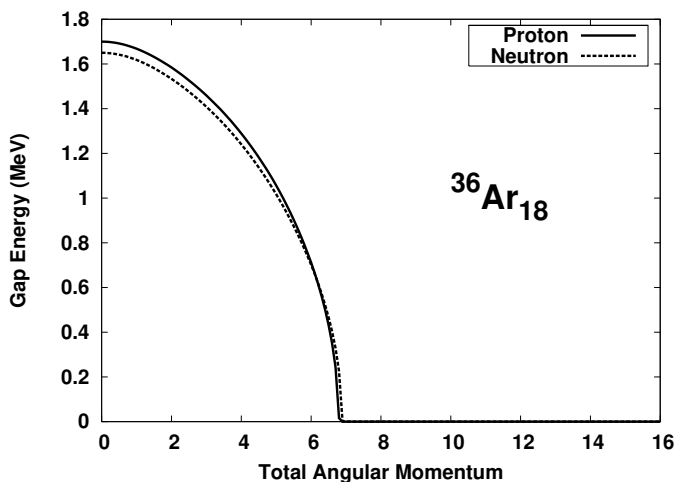


FIG. 10: The pairing-gap energies at the total angular momentum $0 \leq J \leq 16\hbar$. The $g_{9/2}$ orbital is included in the model space.

2. Backbending and roles of the $g_{9/2}$ orbital

To examine the quality of our calculation, it is useful to see the backbending plot first, which is presented in Fig.11. Due to the disappearance of the pairing gap at $J \simeq 7\hbar$, backbending starts earlier (at $J \simeq 7\hbar$) than the experiment (at $J \simeq 10\hbar$). Having accepted this discrepancy, the calculation manages to reproduce the qualitative behavior of the backbending profile of the SD band in this nucleus. Hence, in order to discuss the structural change causing the backbending, it is sufficient to study

Orbital	$d_{5/2}$	$s_{1/2}$	$d_{3/2}$	$f_{7/2}$	$p_{3/2}$	$f_{5/2}$	$p_{1/2}$	$g_{9/2}$
Proton	5.07	1.03	1.23	1.46	0.61	0.12	0.11	0.38
Neutron	5.07	1.03	1.23	1.40	0.65	0.12	0.12	0.36
Total	10.17	2.06	2.46	2.86	1.26	0.24	0.23	0.74

TABLE VII: Occupation numbers of ^{36}Ar at $J = 0$ in the case with the $g_{9/2}$ orbital included in the model space. The subspace ($s_{1/2}d_{3/2}$) is occupied by about four to five (= 4.52) particles, while the pf shell is filled with four to five (= 4.59) particles. The hole occupation number in the $d_{5/2}$ orbital is 1.83 (= $12 - 10.17$).

Orbital	$d_{5/2}$	$s_{1/2}$	$d_{3/2}$	$f_{7/2}$	$p_{3/2}$	$f_{5/2}$	$p_{1/2}$	$g_{9/2}$
Proton	5.42	1.26	1.17	1.86	0.11	0.03	0.00	0.15
Neutron	5.43	1.26	1.17	1.84	0.12	0.03	0.01	0.14
Total	10.85	2.52	2.34	3.70	0.23	0.06	0.01	0.29

TABLE VIII: Occupation numbers of ^{36}Ar at $J = 16\hbar$ in the case with the $g_{9/2}$ orbital included in the model space. The subspace ($s_{1/2}d_{3/2}$) is occupied by about five (= 4.86) particles, while the pf shell is filled with four (= 4.00) particles. The hole occupation number in the $d_{5/2}$ orbital is 1.13 (= $12 - 10.85$).

the configurations before and after $J \simeq 7\hbar$ in our model. Let us see the corresponding occupation numbers next.

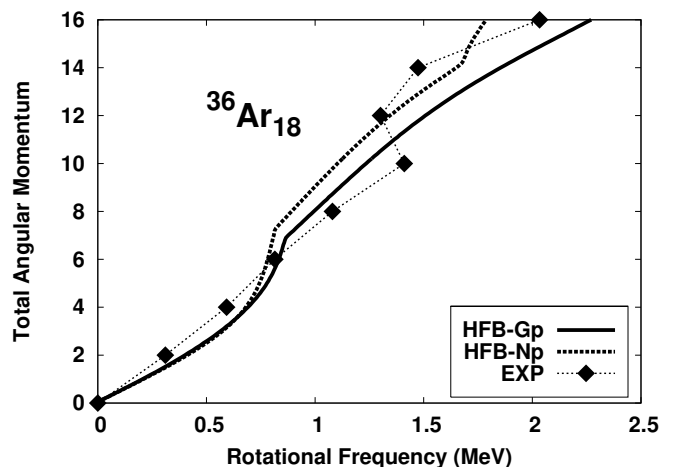


FIG. 11: Backbending plot of the SD band of ^{36}Ar . HFB-Np (HFB-Gp) corresponds to the calculation without (with) the $g_{9/2}$ orbital in the model space.

The occupation numbers are displayed in Fig.12, as well as in Tables VII and VIII. Table VII, which presents the configurations before the backbending, shows that approximately four and a half particles occupy the subspace of the sd shell, as well as the pf shell. The $g_{9/2}$ orbital is occupied by less than one particle, so that the orbital is expected to play only a limited role in the low-spin structure of ^{36}Ar . One can notice that there are

³⁾ The SLy4 parameter results in triaxial deformation for the SD bandhead, but this result may be “less reliable” than the other parameter sets according to the authors [12].

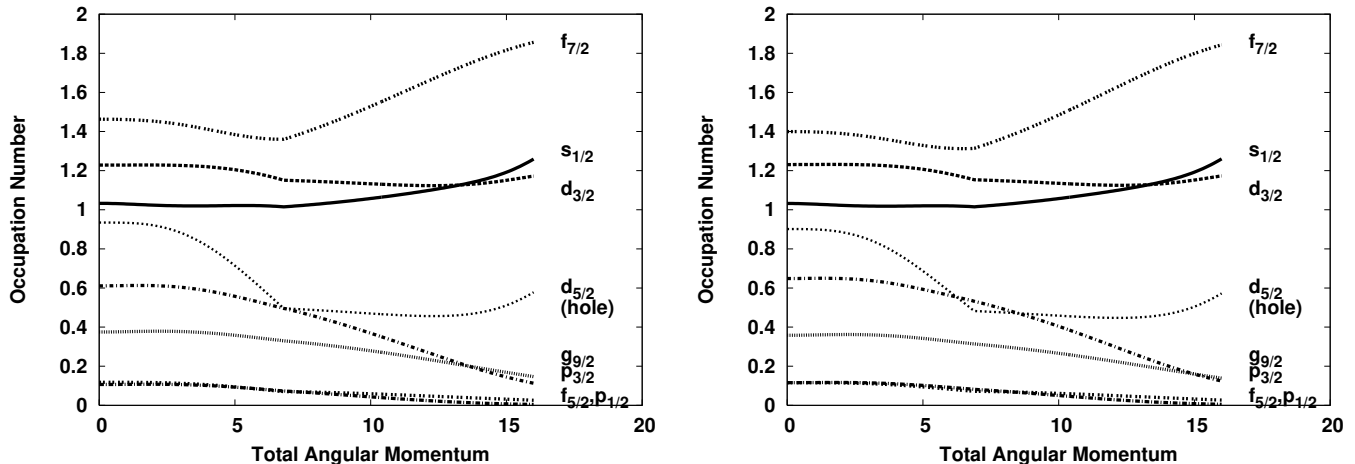


FIG. 12: Proton (left) and neutron (right) occupation numbers as a function of the total angular momentum for ^{36}Ar . In this case, the $g_{9/2}$ orbital is included in the model space.

about two holes in the $d_{5/2}$ orbital. This result implies the structure of $(d_{5/2})^{-2}(s_{1/2}d_{3/2})^{4.5}(fp)^{4.5}(g_{9/2})^1$ at the band head of the SD band, which is similar to the $(s_{1/2}d_{3/2})^4(fp)^4$ structure suggested by the shell model calculation. This structure, which has a configuration of two holes in the $d_{5/2}$ orbital and one particle in the $g_{9/2}$ orbital, is also similar to our result for the bandhead structure of the SD band of ^{40}Ca with the $g_{9/2}$ orbital included in the model space.

Turning a focus onto the higher-spin states inside the SD band, one can tell that the configuration actually turns out to be closer to the configuration suggested by the shell-model calculation. From the Table VIII, our calculation suggests the $(d_{5/2})^{-1}(s_{1/2}d_{3/2})^5(fp)^4$ at $J = 16\hbar$. The $g_{9/2}$ orbital seems to play, again, no role in this case, so that the state resembles the 4p-4h configuration $(s_{1/2}d_{3/2})^4(fp)^4$ in the truncated shell-model diagonalization. From this analysis, we can say that the basic configuration does not change much between before and after the backbending.

Fig.12 also suggests that the $g_{9/2}$ orbital is not a key player for the backbending. Its occupation number is quite low and fairly regular throughout the whole range of the total angular momentum. Instead, the occupation number in the $f_{7/2}$ orbital suddenly starts to increase in the post-backbending region ($J \gtrsim 7\hbar$) to indicate a rotational alignment in this orbital. This result is consistent with the interpretation of the backbending by the PSM [11]. The $s_{1/2}$ orbital also shows the increase, but it is more gradual in comparison to the $f_{7/2}$ orbital. The sharp drop of the hole occupation number in the $d_{5/2}$ orbital can be noticed clearly in the figure. This means that the $d_{5/2}$ orbital starts to be filled by the deexcitations from the upper shells (about a half particle from the $g_{9/2}$ orbital and another half from the pf shells). This result implies that the deformation becomes less substantial and the cross-shell excitation is suppressed to some

extent. We will take a closer look at a relation between the deformation (β) and the position of the $g_{9/2}$ orbital intruding into the sd shell, soon below.

An indication of the decrease in elongation at high spin was reported by other calculations such as the shell-model diagonalization [3], the cranked Skyrme HF calculation [12], and the cranked Nilsson calculation [22]. Fig.13 shows the calculated quadrupole deformation in terms of triaxiality (γ) and elongation (β), with our model. With or without the $g_{9/2}$ orbital in the model space, there is no much difference in the manner of the shape evolution, as already mentioned above. Before the backbending, the system maintains an axially symmetric shape, while triaxial deformation starts to grow after the backbending (in particular, $J \gtrsim 10\hbar$) although the absolute value of γ is less than 10° . The small $|\gamma|$ value explains the reason for the successful descriptions of the PSM calculation [11], as well as the projected GCM calculation [13].

Based on the above discussions, it seems that we can conclude that the $g_{9/2}$ orbital plays no significant role, unlike the ^{40}Ca case. This can be qualitatively explained from two things. One is the position of the Fermi levels, which are lower than the one of the ^{40}Ca . That is, cross-shell excitations cost energetically more in ^{36}Ar than in ^{40}Ca . The other is smaller β value of the quadrupole deformation. From the Nilsson diagram, it can be learned that the $g_{9/2}$ orbital can behave like an intruder orbital when the deformation is as large as $\beta \simeq 0.6$. However, when the deformation becomes smaller such as $\beta \simeq 0.4 - 0.5$, the $g_{9/2}$ orbital remains to be high in energy and the mixture of this orbital to the other orbitals in the sd shell becomes less likely.

If the backbending plot, Fig.11, is carefully studied, however, one can find that there is a little discrepancy in the high-spin behavior of the curves. The second backbending seems to happen at $J \simeq 14\hbar$ in the case without

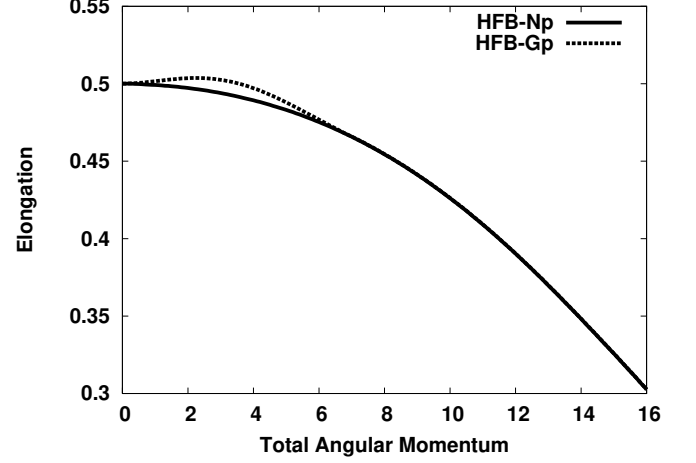
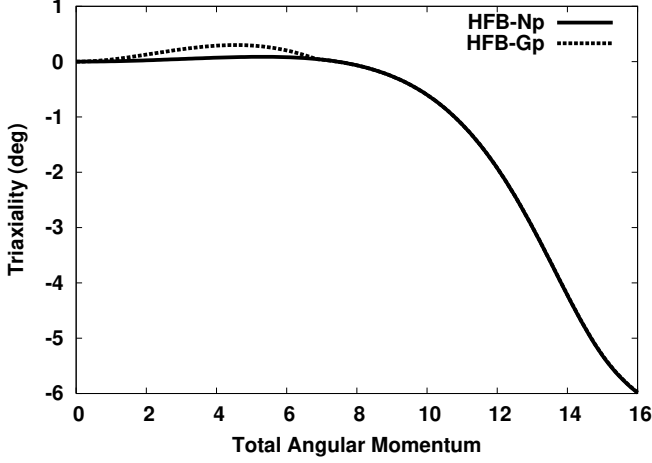


FIG. 13: Calculated triaxiality γ (left panel) and elongation β (right), as functions of the total angular momentum for ^{36}Ar .

Orbital	$d_{5/2}$	$s_{1/2}$	$d_{3/2}$	$f_{7/2}$	$p_{3/2}$	$f_{5/2}$	$p_{1/2}$
Proton	5.38	1.33	1.29	1.95	0.00	0.05	0.00
Neutron	5.38	1.33	1.29	1.95	0.00	0.05	0.00
Total	10.76	2.66	2.58	3.90	0.00	0.10	0.00

TABLE IX: Occupation numbers of ^{36}Ar at $J = 16\hbar$ in the case with the $g_{9/2}$ orbital excluded from the model space. The subspace ($s_{1/2}d_{3/2}$) is occupied by about five ($= 5.24$) particles, while the pf-shell is filled with four ($= 4.00$) particles. The hole occupation number in the $d_{5/2}$ excluded is 1.24 ($= 12 - 10.76$).

the $g_{9/2}$ orbital (HFB-Np). Obviously, this result is inconsistent with the experimental data, showing no sign of the second backbending. The case with the $g_{9/2}$ orbital (HFB-Gp) shows the closer results to the experiment. Apparently from the analyses of the occupation numbers and the deformation evolution, the $g_{9/2}$ orbital plays no active role in the SD structure. But it seems that these results does not mean that one can exclude the $g_{9/2}$ orbital from the model space.

Let us examine how this discrepancy happens. First of all, let us compare the occupation numbers in these two cases (i.e., HFB-Gp and HFB-Np) at $J = 16\hbar$. The case with the $g_{9/2}$ orbital (HFB-Gp) is already shown in Table VIII, whereas the case without the $g_{9/2}$ orbital (HFB-Np) is presented in Table IX. No significant difference can be seen from these two Tables. Only a tiny difference can be seen that the concentration onto the $f_{7/2}$ orbital is slightly higher in the latter case than the former.

It is then worth a look at the single-particle spin component along the cranking axis. There are differences between the two cases, which are found in the $f_{7/2}$ and $d_{5/2}$ orbitals at $J \gtrsim 14\hbar$. Their behaviors are plotted in Fig.14. Obviously, the $g_{9/2}$ orbital is not involved in the production of angular momentum. The low occupation

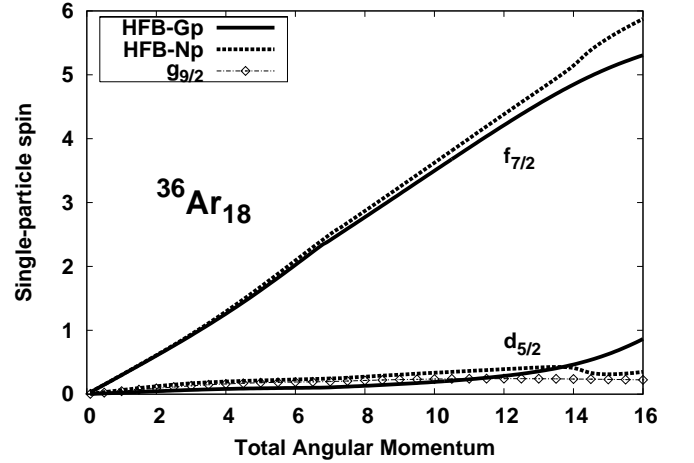


FIG. 14: Single-particle spin components along the cranking axis. Only the $f_{7/2}$ and $d_{5/2}$ orbitals for protons are plotted to compare the two cases (with and without the $g_{9/2}$ in the model space).

number in this orbital implies the consistency with the case without the $g_{9/2}$ orbital. On the other hand, $f_{7/2}$ and $d_{5/2}$ orbitals show slightly different behaviors in the two cases (HFB-Gp and -Np in the figure, which correspond to the case with and without the $g_{9/2}$ orbital in the model space). When the $g_{9/2}$ orbital is removed from the model space, the alignment in the $f_{7/2}$ orbital is slightly accelerated beyond $J = 14\hbar$. Whereas, in the other case, the alignment of the $f_{7/2}$ orbital slows down a little. The opposite behavior is seen in the $d_{5/2}$ orbitals. From this analysis, it can be said that the further alignment in the $f_{7/2}$ orbital causes the second backbending when the $g_{9/2}$ orbital is absent. This backbending should be regarded as an artifact and it is caused by the secondary effect due to the lack of the $g_{9/2}$ orbital, which creates subtle differences from the case with the $g_{9/2}$ orbital.

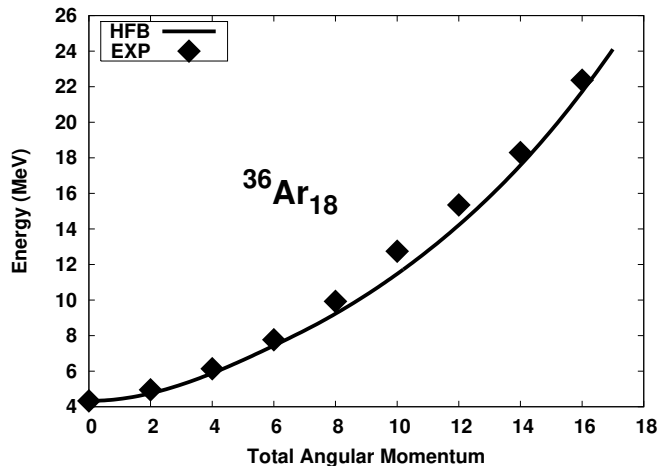


FIG. 15: Calculated and observed rotational energies of the SD band in ^{36}Ar . The $g_{9/2}$ orbital is taken into account in the model space. The calculated ground-state energy (at $J = 0$) is normalized with the experimental value, $E(J = 0) = 4.3291$ MeV.

Therefore, despite the discrepancy in Fig.11, our previous conclusion, that is, the $g_{9/2}$ orbital plays no major role in the SD band of ^{36}Ar , still holds because the qualitative characters of the SD structure does not change whether the $g_{9/2}$ orbital is considered or not. It is true, however, that a better description demands an inclusion of the $g_{9/2}$ orbital in the model space, particularly for the backbending plot.

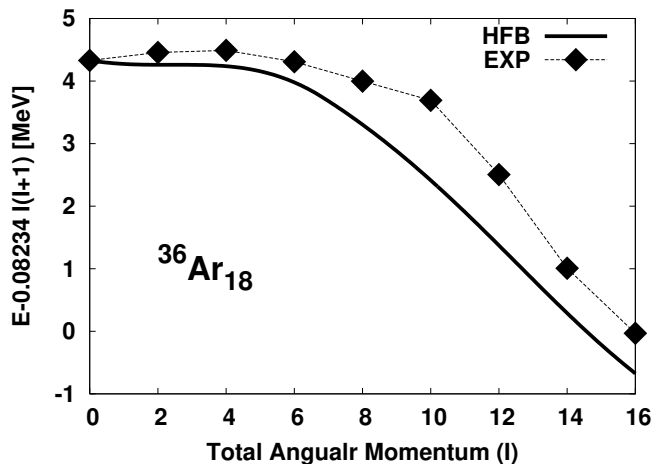


FIG. 16: Excitation energies relative to a rigid-rotor energy, $E_R = aJ(J + 1)$, where $a = 0.08234$ (MeV), for ^{36}Ar .

3. Pairing correlation and band termination

Let us now compare the energy spectrum between the calculation and the experimental data, which are shown in Figs.15 and 16. Discrepancies are seen in the back-

bending region ($8\hbar \lesssim J \lesssim 12\hbar$). As we have discussed earlier, these discrepancies are the result of the pairing collapse (See also Fig.10). But the qualitative behavior is managed to be reproduced. In particular, the plateau structure at low spin and a sharp slope at high spin are well reproduced in Fig.16. In comparison with the cranked Nilsson calculation in Ref.[1], our result shows an improvement as a mean-field approach, which takes into account the pairing.

Without the pairing, the cranked Nilsson calculation suggests an occurrence of the band-termination phenomenon for the SD band of ^{36}Ar [22]. The typical feature of the band termination appears as a shape change into oblate deformation. Earlier in the present study, we have learned that the triaxial deformation is suppressed with a proper treatment of the pairing (Fig.13). It is interesting to study if the band termination and the associated oblate deformation can emerge in the absence of the pairing in our model.

By choosing the initial pairing-gap parameters to be very weak, that is, $(\Delta_p^0, \Delta_n^0) = (0.15, 0.15)$ MeV, the effect of the pairing correlation is examined in the following calculation. (The $g_{9/2}$ orbital is included in this analysis.) This choice of the initial parameters causes the breakdown of the pairing as early as at $J \simeq 1.5\hbar$. Effectively, the calculation turns to be the HF calculation beyond this total angular momentum, which can be comparable with the cranked Nilsson calculation without the pairing. The corresponding cranking calculation gives regular solutions until $J = 16\hbar$, the band termination point. But beyond the termination point, the solution becomes irregular and shows unphysical behavior, so that we ignore the calculations beyond the band termination point in this analysis.

In the band termination spin ($J = 16\hbar$), the occupation numbers of the $f_{7/2}$ orbital are calculated to be 1.94 each for neutrons and protons. Therefore, the net particles occupying the $f_{7/2}$ orbital are four (i.e., $= 2 + 2$), and the result is consistent with the shell model configuration. Two particles occupying the $f_{7/2}$ orbital can generate the maximum angular momentum of $J = 6\hbar$, which corresponds to the band termination.

In Fig.17, the calculated single-particle alignments are plotted for protons and neutrons. Our calculation (without the pairing) reproduces the above situation: the single-particle angular momentum carried by the $f_{7/2}$ orbital is almost $12\hbar$, consisting of $6\hbar$ for protons and $6\hbar$ for neutrons.

In Fig.18, the calculated quadrupole deformation, that is, triaxiality (γ) and elongation (β), are plotted. The profile for the elongation does not change from the previous case with the pairing correlation. However, the behavior of the triaxial evolution is different, especially beyond $J = 12\hbar$. At the band termination point, the value of γ reaches -60° , indicating the non-collective oblate shape. From this analysis relying on the self-consistent cranking calculation, it is confirmed that the band termination phenomenon happens when the pairing correlation

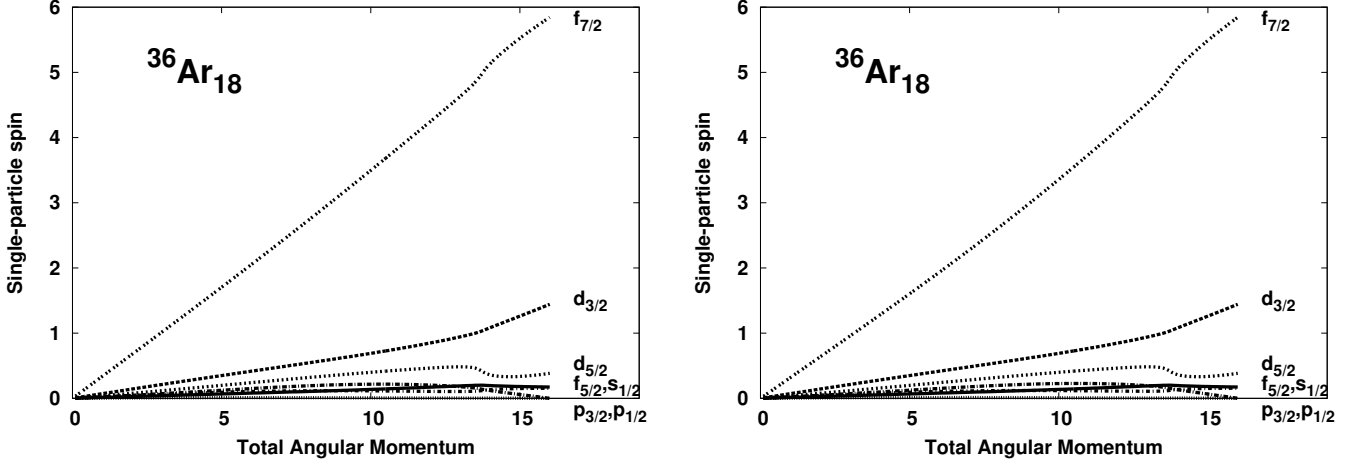


FIG. 17: Proton (left) and neutron (right) single-particle spin components along the cranking axis for ^{38}Ar . The $g_{9/2}$ orbital is included in the model space.

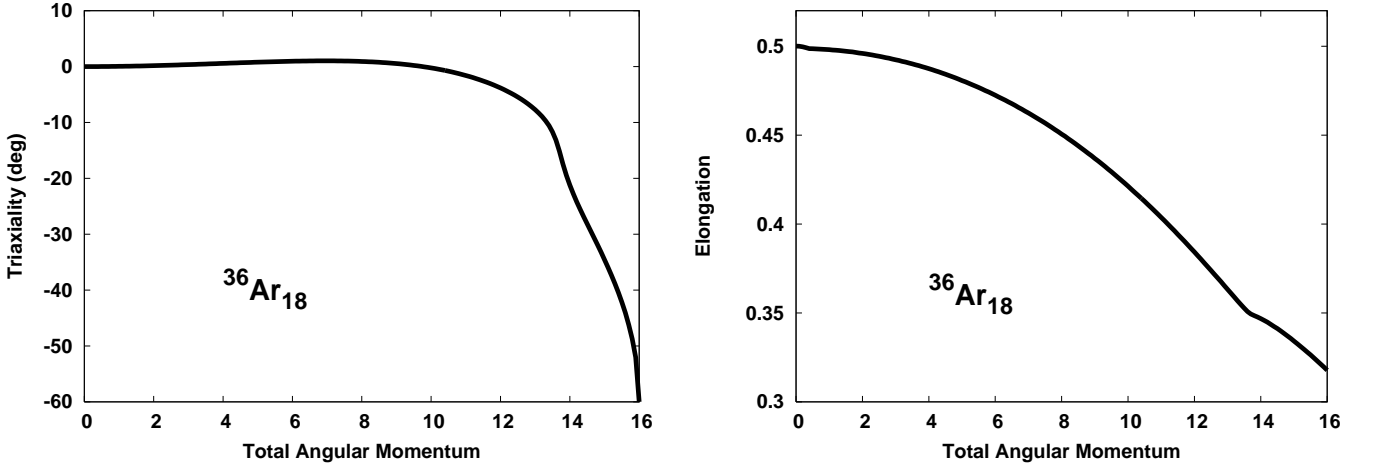


FIG. 18: Calculated triaxiality γ (left panel) and elongation β (right), as functions of the total angular momentum for ^{36}Ar , when the pairing correlation is switched off.

is absent from the system (or very weak).

4. Summary for ^{36}Ar

As a partial summary for ^{36}Ar , we can conclude that the previously proposed structure, $(s_{1/2}d_{3/2})^4(fp)^4$, seems to be a good approximation for the structure of ^{36}Ar , according to our results. It is suggested that backbending in the SD band of ^{36}Ar is caused by the alignment in the $f_{7/2}$ orbitals, as concluded by the PSM calculation [11]. The $g_{9/2}$ orbital does not play any significant role. From the successful description of the SD band at low spin and the failure in the backbending region, it was demonstrated that the pairing correlation is very important to describe the structure of the SD band. Triaxial deformation starts to occur at high spin, but the

degree of triaxiality is not so substantial that the SD states are well described as an axially symmetric nuclear many-body system.

IV. CONCLUSIONS

The self-consistent cranking calculation based on the HFB method was applied to the superdeformed bands of two $N = Z$ nuclei, ^{40}Ca and ^{36}Ar . Our microscopic calculations with the P+Q·Q interaction can manage to give good qualitative explanations (occasionally quantitatively) to the energy spectrum, rotational alignment, and backbending phenomenon of these nuclear systems.

Special attentions were paid to the roles of (1) the $d_{5/2}$ orbital, which was removed from the sd-pf model space in the shell-model diagonalizations; and (2) the $g_{9/2}$ or-

bital, which belongs to a higher shell ($N = 4$) than the sd-pf shell. The effect of the pairing correlation was also investigated in connection to the evolution of triaxial deformation and the band termination phenomenon.

Inside the framework of our model, it was found that the truncation of the $d_{5/2}$ orbital can be justified as far as lower-spin states are considered. Whereas, high-spin states are found to be produced due to a gradual excitation from the $d_{5/2}$ orbital to the upper sd shell. However, in either case of ^{40}Ca and ^{36}Ar , an inclusion of the $d_{5/2}$ orbital does not affect the nuclear structure of the SD states very much.

On the contrary, the $g_{9/2}$ orbital was found to change the nuclear structure drastically for ^{40}Ca : backbending may happen at $J \simeq 20\hbar$. However, the orbital plays no significant role for ^{36}Ar . These differences come from the location of the Fermi levels and the deformation (β), which is $\simeq 0.6$ for ^{40}Ca while $\simeq 0.4$ for ^{36}Ar . This difference influences the position of the $g_{9/2}$ orbital as an “intruder orbital” into the sd shell, in terms of the deformed Nilsson model.

The pairing correlation was found to be important to produce a proper energy spectrum and tend to act as a suppressor of triaxial deformation. Without the pairing, triaxial deformation would be enhanced and the non-collective oblate shape ($\gamma = -60^\circ$) would ultimately

emerge at high spin. However, in our model taking the pairing correlation into account, it is observed that triaxiality is suppressed to $|\gamma| \lesssim 10^\circ$. In this sense, the SD states of both ^{40}Ca and ^{36}Ar are nearly axial symmetric in our model, which can justify other calculations assuming the axial symmetry.

Despite the success for the qualitative explanations, a problem was recognized in relation to the pairing collapse at high spin. An improvement is surely necessary for more accurate and quantitative descriptions of the high-spin structure, especially around the backbending region.

Nevertheless, through this work, the P+Q-Q model based on the cranked HFB approach was demonstrated to be a practical and effective model to describe high-spin nuclear structure showing superdeformation.

Acknowledgments

M.O. appreciates useful discussions with S. Williams, E. Ideguchi, T. Shizuma, N. Onishi and N. Timofeyuk. The author thanks P. M. Walker for his careful reading of the manuscript. This work is supported by STFC/EP SRC with an advanced research fellowship GR/R75557/01 as well as a first grant EP/C520521/1.

-
- [1] C. E. Svensson, A. O. Macchiavelli, A. Juodagalvis, A. Poves, I. Ragnarsson, S. Åberg, D. E. Appelbe, R. A. E. Austin, C. Baktash, G. C. Ball, M. P. Carpenter, E. Caurier, R. M. Clark, M. Cromaz, M. A. Deleplanque, R. M. Diamond, P. Fallon, M. Furlotti, A. Galindo-Uribarri, R. V. F. Janssens, G. J. Lane, I. Y. Lee, M. Lipoglavsek, F. Nowacki, S. D. Paul, D. C. Radford, D. G. Sranites, D. Seweryniak, F. S. Stephens, V. Tomov, K. Vetter, D. Ward, and C.H. Yu, *Phys. Rev. Lett.* **85**, 2693 (2000).
- [2] E. Ideguchi, D. G. Sarantites, W. Reviol, A. V. Afanasjev, M. Devlin, C. Baktash, R. V. F. Janssens, D. Rudolph, A. Axelsson, M. P. Carpenter, A. Galindo-Uribarri, D. R. LaFosse, T. Lauritsen, F. Lerma, C. J. Lister, P. Reiter, D. Seweryniak, M. Weiszflog, and J. N. Wilson, *Phys. Rev. Lett.* **87**, 222501 (2001).
- [3] A. Poves, *Nucl. Phys. A* **731**, 339 (2004).
- [4] For example, M. Bender, P.-H. Heenen, P.-G. Reinhard, *Rev. Mod. Phys.* **75**, 121 (2003).
- [5] B. Singh, R. B. Firestone, and S. Y. Frank Chu, *Table of Superdeformed Nuclear Bands and Fission Isomers*, LBL-38004, (1997).
- [6] H.-Q. Jin, C. Baktash, M. J. Brinkman, C. J. Gross, D. G. Sarantites, I. Y. Lee, B. Cederwall, F. Cristancho, J. Doring, F. E. Durham, P.-F. Hua, G. D. Johns, M. Korolija, D. R. LaFosse, E. Landulfo, A. O. Macchiavelli, W. Rathbun, J. X. Saladin, D. W. Stracener, S. L. Tabor, and T. R. Werner, *Phys. Rev. Lett.* **75**, 1471 (1995).
- [7] P. J. Twin, B. M. Nyako, A. H. Nelson, J. Simpson, M. A. Bentley, H. W. Cranmer-Gordon, P. D. Forsyth, D. Howe, A. R. Mokhtar, J. D. Morrison, J. F. Sharpey-Schafer, G. Sletten, *Phys. Rev. Lett.* **57**, 811 (1986).
- [8] K. Theine, F. Hannachi, P. Willsau, H. Hubel, D. Mehta, W. Schumitz, C. X. Yang, D. B. Fossan, H. Grawe, H. Kluge, K. H. Maier, *Z. Phys. A* **336**, 113 (1990).
- [9] E. Caurier, F. Nowacki, and A. Poves, *Phys. Rev. Lett.* **95**, 042502 (2005).
- [10] E. Caurier, J. Menendez, F. Nowacki, and A. Poves, *Phys. Rev. C* **75**, 054317 (2007).
- [11] G.-L. Long and Y. Sun, *Phys. Rev. C* **63**, 021305(R) (2001).
- [12] T. Inakura, S. Mizutori, M. Yamagami, and K. Matsuyanagi, *Nucl. Phys. A* **710**, 261 (2002).
- [13] M. Bender, H. Flocard, and P.-H. Heenen, *Phys. Rev. C* **68**, 044321 (2003).
- [14] T. Horibata, N. Onishi, *Nucl. Phys. A* **596**, 251 (1996).
- [15] S. G. Nilsson, I. Ragnarsson, *Shapes and Shells in Nuclear Structure*, Cambridge University Press, Cambridge (1995).
- [16] T. Bengtsson, I. Ragnarsson, *Nucl. Phys. A* **436**, 14 (1985).
- [17] K. Kumar and M. Baranger, *Nucl. Phys. A* **110**, 490 (1968).
- [18] P. Möller, J. R. Nix, W. D. Meyer, and W. J. Swatecki, *At. Data Nucl. Data Tables* **59**, 185 (1995).
- [19] P. Ring and P. Schuck, *Nuclear Many-body Problem*, Springer-Verlag, Berlin (1980).
- [20] H. C. Pradhan, Y. Nogami, and J. Law, *Nucl. Phys. A* **201**, 357 (1972).
- [21] D. L. Hill and J. A. Wheeler, *Phys. Rev.* **89** 106 (1952).
- [22] C. E. Svensson, A. O. Macchiavelli, A. Juodagalvis, A. Poves, I. Ragnarsson, S. Åberg, D. E. Appelbe, R. A. E. Austin, C. Baktash, G. C. Ball, M. P. Carpenter, E.

Caurier, R. M. Clark, M. Cromaz, M. A. Deleplanque, R. M. Diamond, P. Fallon, M. Furlotti, A. Galindo-Uribarri, R. V. F. Janssens, G. J. Lane, I. Y. Lee, M. Lipoglavsek, F. Nowacki, S. D. Paul, D. C. Radford, D. G. Sranites,

D. Seweryniak, F. S. Stephens, V. Tomov, K. Vetter, D. Ward, and C.H. Yu, *Acta. Phys. Pol.* **32**, 2413 (2001).